Acta Crystallographica Section A
Foundations of Crystallography
ISSN 0108-7673

Received 18 May 2011
Accepted 22 July 2011

A Fourier transform method for powder diffraction based on the Debye scattering equation

Noel William Thomas

Fachhochschule Koblenz, Fachbereich Ingenieurwesen, Fachrichtung Werkstofftechnik Glas und Keramik, Rheinstrasse 56, 56203 Höhr-Grenzhausen, Germany. Correspondence e-mail: thomas@fh-koblenz.de

A fast Fourier transform algorithm is introduced into the method recently defined for calculating powder diffraction patterns by means of the Debye scattering equation (DSE) [Thomas (2010). *Acta Cryst.* A**66**, 64–77]. For this purpose, conventionally used histograms of interatomic distances are replaced by compound transmittance functions. These may be Fourier transformed to partial diffraction patterns, which sum to give the complete diffraction pattern. They also lead to an alternative analytical expression for the DSE sum, which reveals its convergence behaviour. A means of embedding the DSE approach within the reciprocal-lattice–structure-factor method is indicated, with interpolation methods for deriving the peak profiles of nanocrystalline materials outlined. Efficient calculation of transmittance functions for larger crystallites requires the Patterson group symmetry of the crystals to be taken into account, as shown for α- and β-quartz. The capability of the transmittance functions to accommodate stacking disorder is demonstrated by reference to kaolinite, with a fully analytical treatment of disorder described. Areas of future work brought about by these developments are discussed, specifically the handling of anisotropic atomic displacement parameters, inverse Fourier transformation and the incorporation of instrumental (diffractometer) parameters.

1. Introduction

There has been a resurgence of interest in the application of the Debye scattering equation (DSE) [equation (1)][1] to powder diffraction in the past 20 years,

$$I^{\rm Debye}(Q) = \sum_m \sum_n f_m f_n \frac{\sin(Q r_{mn})}{Q r_{mn}}. \qquad (1)$$

This has been stimulated by the steady growth both in computing power and in the technological importance of nanomaterials.

The mathematical connection between the DSE and the fast Fourier transform (FFT) was first exploited by Hall & Monot (1991), who outlined an FFT-based procedure for large clusters based on two key elements: (*a*) the discretization of interatomic distances in the form of a histogram ($R = j\Delta R$; $j = 1, N$); (*b*) interpolation of the discrete points in Q space generated by the FFT. The use of FFT methods in connection with the DSE was taken up again by Cervellino *et al.* (2006), who introduced a broadening function, such as a Gaussian, which could be convoluted with the interatomic distance histograms in order to generate a continuous function for Fourier transformation. The latter function could be sampled with a significantly higher sample width, ΔR, leading to significant reductions in computer time for the FFT operation. Furthermore, the influence of the broadening function on the diffraction pattern could be corrected for by means of multiplying factors, which were applied to the Fourier transform at discrete points in Q space. The parameterization of the broadening functions also permitted the level of accuracy of the calculations to be traded off against computer time. This enabled the aim of very fast calculations for nanoclusters to be realized, such as might be required in least-squares minimization procedures. Attention was also given to the possible use of Chebyshev polynomials as a more efficient alternative to the FFT. The innovative methods of these authors have, since then, matured into the computer package called *DEBUSSY* (Cervellino *et al.*, 2010). As an alternative, hardware-led approach towards optimizing DSE calculations, by comparison, Gelisio *et al.* (2010) have demonstrated the potential of graphics processing units (GPU) compared to central processing units (CPU). A further focus of activity in connection with the DSE concerns its ability to model particle size distributions (Beyerlein *et al.*, 2009).

An independent contribution towards this growing DSE effort was made by Thomas (2010), who sought to extend the use of the DSE to larger crystallites, such as might occur for clay minerals such as kaolinite. Furthermore, the capability of

[1] $I^{\rm Debye}(Q)$ is the intensity of radiation scattered in a direction at an angle of 2θ to the incident beam, whereby $Q = (4\pi \sin\theta)/\lambda$. The double summation is carried out over all atoms m and n within a single crystallite, with f_m and f_n atomic scattering factors.

Table 1
Independent Patterson vectors in sodium chloride.

The entry in column 'P' gives the number of times the vector contributes to the complete set of Patterson vectors, of which there are 64 in all.

	x	y	z	Length (Å)	P	Identity
Set 1						$Fm\bar{3}m$ 4*a* (1)
1	0	0	0	0	8	Na···Na, Cl···Cl
Set 2						$Fm\bar{3}m$ 4*b* (1)
2	$\frac{1}{2}$	0	0	2.820	8	Na···Cl
3	0	$\frac{1}{2}$	0	2.820	8	Na···Cl
4	0	0	$\frac{1}{2}$	2.820	8	Na···Cl
Set 3						$Fm\bar{3}m$ 4*a* (2)
5	0	$\frac{1}{2}$	$\frac{1}{2}$	3.988	4	Na···Na, Cl···Cl
6	$\frac{1}{2}$	0	$\frac{1}{2}$	3.988	4	Na···Na, Cl···Cl
7	$\frac{1}{2}$	$\frac{1}{2}$	0	3.988	4	Na···Na, Cl···Cl
8	0	$-\frac{1}{2}$	$\frac{1}{2}$	3.988	4	Na···Na, Cl···Cl
9	$-\frac{1}{2}$	0	$\frac{1}{2}$	3.988	4	Na···Na, Cl···Cl
10	$-\frac{1}{2}$	$\frac{1}{2}$	0	3.988	4	Na···Na, Cl···Cl
Set 4						$Fm\bar{3}m$ 4*b* (2)
11	$\frac{1}{2}$	$\frac{1}{2}$	$\frac{1}{2}$	4.884	2	Na···Cl
12	$-\frac{1}{2}$	$\frac{1}{2}$	$\frac{1}{2}$	4.884	2	Na···Cl
13	$\frac{1}{2}$	$-\frac{1}{2}$	$\frac{1}{2}$	4.884	2	Na···Cl
14	$-\frac{1}{2}$	$-\frac{1}{2}$	$\frac{1}{2}$	4.884	2	Na···Cl

treating more complex chemical compositions was seen as desirable. The fundamental method for optimizing computational speed here presupposed the existence of perfect crystallinity, although point defects and stacking faults could also be accommodated. The central method employed was to split each vector linking pairs of atoms within the generating crystal into two parts, *i.e.* a lattice vector and a Patterson vector. Thereafter the frequencies of occurrence of the different lattice vectors $N(n_x, n_y, n_z)$ could be expressed as a function of crystallite size and shape, by means of the parameters L_x, L_y, L_z, the number of unit cells in the x, y and z directions [equation (2)]:

$$N(n_x, n_y, n_z) = \frac{1}{\left[N_{\rm uc}\, V_{\rm uc}\right]}\left(1 - \frac{|n_x|}{L_x}\right)\left(1 - \frac{|n_y|}{L_y}\right)\left(1 - \frac{|n_z|}{L_z}\right). \quad (2)$$

Here $0 \leq |n_x| < L_x$, $0 \leq |n_y| < L_y$ and $0 \leq n_z < L_z$. The factor $1/[N_{\rm uc}\, V_{\rm uc}]$, with $N_{\rm uc}$ the number of atoms in the unit cell and $V_{\rm uc}$ its unit volume, serves to express the calculated intensities in units per atom.

In common with the work of other authors, a histogram representation of interatomic distances was used, in this case with a fixed sample width, Δr, of 0.01 Å. The DSE sum was evaluated from histograms of different atom-pair types at discrete, closely spaced Q values by calculating factors $p_{sj}[\sin(Qj\Delta r)/Qj\Delta r]$ directly (s, pair type; j, bin index; p_{sj}, bin occupancy). This method was also used as a benchmarking exercise by Hall & Monot (1991) and by Cervellino *et al.* (2006), in order to monitor the comparative performance of FFT procedures.

Although the aim was reached in the earlier article (Thomas, 2010) of applying the DSE to crystallites of length up to 200 nm on a conventional personal computer, there are several points at which improvements in method are called for, in order to benefit computational speed. First, as is well known, the explicit, histogram-based sum of $\mathrm{sinc}(Qr_{mn})$ terms can be optimized by the use of Fourier methods. Secondly, the speed of calculation of the bin occupancies of interatomic distance histograms can be improved by exploiting the symmetry of the set of Patterson vectors of a crystal.

The implementation of these improvements forms the basis of this article. In §2, the FFT method is defined, with NaCl used as a model system, although the principles are valid for all crystalline systems. In §3, the space symmetrical consequences of the fundamental lattice vector–Patterson vector splitting proposed in the earlier article (Thomas, 2010) are drawn, by referring to the structures of α- and β-quartz.[2] Again, the principles are of global validity for perfectly crystalline systems. There are three parts that deviate from the mainstream: §4, §2.6, §2.7. The material in §4 is a solution to a problem thrown up in the earlier article, in which random-number generators were found to generate noisy diffraction patterns for disordered kaolinite. In §2.6 and §2.7, some consequences of the new FFT method are explored analytically, these being relevant for future work.

2. Definition of the Fourier transform method

2.1. The structure of sodium chloride and the identification of equivalent sets of Patterson vectors

Sodium chloride is ideally suited as a model system for defining the Fourier transform (FT) method, since the high symmetry of its structure allows a concise handling of the key points. By taking the structure of Walker *et al.* (2004) as a basis, for which the space group is $Fm\bar{3}m$ and a is equal to 5.6401 Å, a set of 14 independent Patterson vectors can be generated, as listed in Table 1. These comprise four different sets, within which the Patterson vectors are of equal length. The full set of vectors can be generated by applying the inversion operation to the listed coordinates.

2.2. The Fourier transform of a slit function and its relevance to the DSE

Although Hall & Monot (1991) and Cervellino *et al.* (2006) utilized odd functions for Fourier transformation in their work, the connection between the DSE and Fourier transform theory can also be made by considering the standard result for the FT of a rectangular slit. This arises frequently in the theory of Fraunhofer diffraction (see, for example, Lipson & Lipson, 1981), and leads to an even function.

Proceeding from the definition of an FT [equation (3)], the integral in equation (4), in which the function to be transformed corresponds to a rectangular slit of transmittance T and width $2R$, results in a $\mathrm{sinc}(QR)$ function multiplied by the factor $2RT$:

[2] Since the methods of §3 apply to the first stage of the DSE calculation (sampling histogram), and the methods of §2 to the second stage (sinc sum/Fourier transform), they could be read in reverse order.

$$F(Q) = \int_{-\infty}^{\infty} f(r)\exp(-iQr)\,\mathrm{d}r \qquad (3)$$

$$F^{\mathrm{slit}}(Q) = \int_{-R}^{R} T\exp(-iQr)\,\mathrm{d}r = 2RT\frac{\sin QR}{QR}. \qquad (4)$$

A comparison of equations (1) and (4) leads to the conclusion that a single interaction between a pair of atoms of length R is mathematically equivalent to a single, simple rectangular slit in Fraunhofer diffraction (Fig. 1). A pairwise interaction of length $R = r_{mn}$ is equivalent to a slit of width $2r_{mn}$ and transmittance $T = f_m f_n/2r_{mn}$.

Owing to the linearity of the FT and the DSE it is possible to transform many different slits (or, equivalently, pairwise atomic interactions) simultaneously. The natural choice is to transform the pairwise interactions resulting from all the lattice vectors arising in the crystal with each set of Patterson vectors separately. This is because each set of Patterson vectors is, in general, associated with different products of scattering factors, $f_m f_n$. In addition, the Q dependence of scattering factors dictates that values of one are assumed for f_m and f_n prior to transformation, such that each interaction of length r_{mn} corresponds to an elementary slit of transmittance $1/(2r_{mn})$. A correction for the real $f_m f_n$ values and their Q dependence is carried out on the Fourier transform, $F(Q)$.

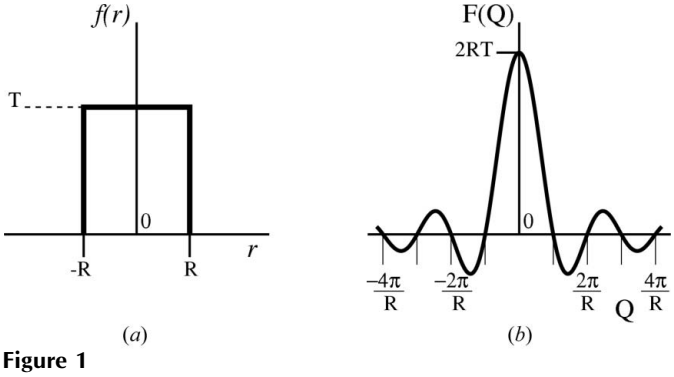

Figure 1
(*a*) A simple diffracting slit of width $2R$ and transmittance T. (*b*) The FT of this slit.

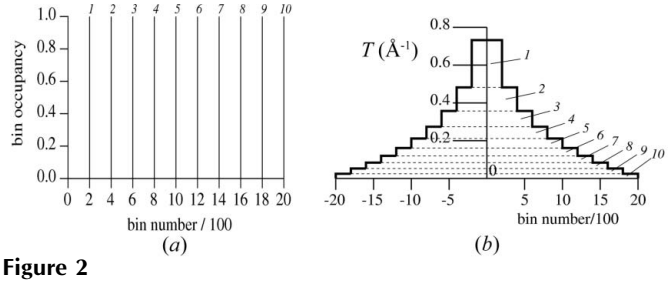

Figure 2
(*a*) A fictitious, unrealistic pair distance histogram consisting of equally spaced occupied bins of occupancy 1.0, which are numbered 1 to 10. (*b*) Representation of this information as a compound diffracting slit of transmittance T. The regions 1 to 10, which are separated by dashed lines, correspond to the contributions of bins 1 to 10 in (*a*) to the resulting monotonically decreasing function.

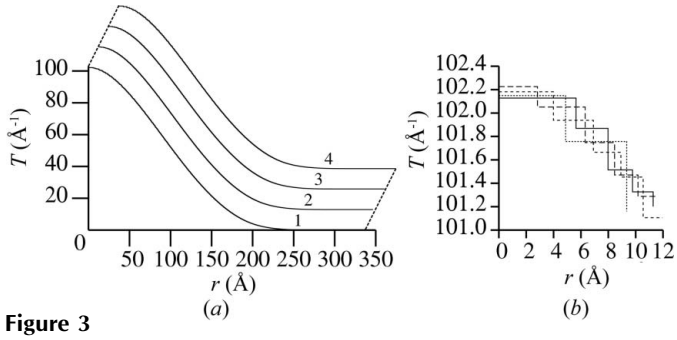

Figure 3
(*a*) Transmittance functions for Patterson vector sets 1 to 4 of a NaCl crystal of dimensions $(20\ \mathrm{nm})^3$. [Scaling per Patterson vector according to equation (2), but with factor $N_{\mathrm{uc}}V_{\mathrm{uc}}$ omitted.] (*b*) Fine structure of curves in (*a*) for interaction lengths of up to 12 Å. (Solid line: Patterson set 1, followed by sets 2 to 4 in order of decreasing dash length.)

Thus, in the case of NaCl, four separate Fourier transforms are carried out, one per set of Patterson vectors in Table 1.

2.3. The equivalence of pair distance histograms and compound diffracting slits

Since a pair distance histogram represents a collection of pair interactions with different frequencies of occurrence, it can be recast into an equivalent function that is obtained by a summation of rectangular functions corresponding to simple diffracting slits.[3] By taking unitary values of the scattering factors f_m and f_n, each single interaction in the pair distance histogram of length R may be taken to correspond to a simple diffracting slit of height $1/2R$. The generation of an equivalent slit-based function from an example pair distance histogram is shown in Fig. 2.

The name 'compound diffraction slit' may be chosen to represent this transmittance function (Fig. 3*b*), which, like the elementary slit of Fig. 2(*a*), is even. It may be visualized as a wide slit with variable transmittance, T. It is seen how the $1/2R$ scaling of the heights of the elementary contributions leads to variable step heights, with the largest step arising from the elementary slit with bin number 200 and the smallest step for the slit with bin number 2000. In realistic pair distance histograms, the step heights are also scaled by the bin occupancies. Since the FT of such a transmittance function will consist of a sum of sinc(Qr) terms, *i.e.* $\sum_i[\sin(Q\,r_i)/Q\,r_i]$, the recasting of histogram information in the form of Fig. 3(*b*) leads to a computationally efficient method of carrying out the Debye sum [equation (1)].

This procedure may be demonstrated for a real system by taking a small crystallite of sodium chloride of dimensions 20 × 20 × 20 nm, this giving rise to 35 × 35 × 35 = 42875 unit cells in total. Four compound diffracting slit functions are

[3] In the earlier article (Thomas, 2010), the term 'pair distribution function' (p.d.f.) was used instead of 'pair distance histogram'. The notation adopted here is more in keeping with accepted practice (see, for example, Hall & Monot, 1991). The term 'p.d.f.', represented as $G(r)$, is more commonly used to describe a function that is derived by inverse Fourier transformation of a total scattering structure function, $S(Q)$, which is derived from diffraction data. For the purposes of calculating $G(r)$ from a known structural model, atomic scattering factors are taken into account as well as pair distances (see, for example, Farrow *et al.*, 2007).

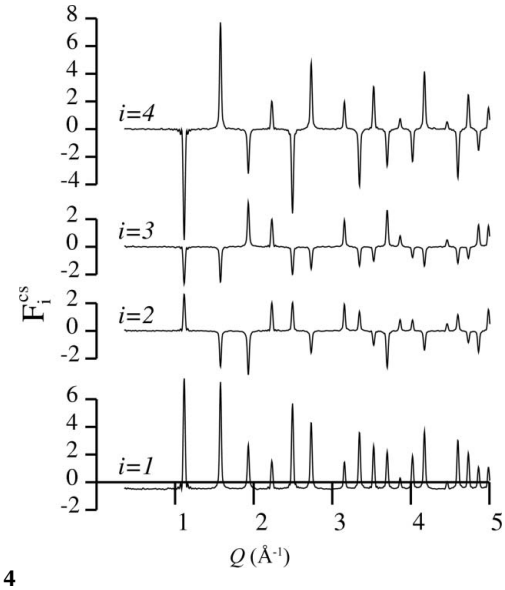

Figure 4
Fourier transforms $F_i^{cs}(Q)$ (i = 1, 4) of the four curves in Fig. 3(*a*) (cs = compound slit).

obtained, one for each set of Patterson vectors in Table 1 (Fig. 3). Since these functions are always even, it is only necessary to consider positive values of interaction distance r explicitly.

Whereas the coarse structure of all four curves in Fig. 3(*a*) is smooth and similar, the fine structure arising from the four different sets of Patterson vectors shows considerable variation (Fig. 3*b*). And whereas Cervellino *et al.* (2006) generated continuous functions for Fourier transformation through the introduction of Gaussian broadening functions, the transmittance functions derived here decrease monotonically with r, with discontinuous steps at the interatomic distances.[4]

2.4. Fourier transforms of the four compound diffracting slits arising for NaCl

Fourier transforms of the slit transmittance functions of Fig. 3(*a*) are shown in Fig. 4. The routine *realft* specified by Press *et al.* (1996) was used for these calculations. A sampling width of 0.01 Å, as in the previous work (Thomas, 2010), led to discrete Q values of spacing 1.198×10^{-3} Å^{-1} for an array size of 2^{19}. These are sufficiently closely spaced to make the use of an interpolation function, as in the work of Hall & Monot (1991), redundant.

Whereas Patterson set 1 just gives rise to peaks, the other three sets give rise to both peaks and troughs at the same Q values. Since the single vector in set 1 is equal to 000, the FT for this set originates from vectors linking the corners of the unit cells, *i.e.* from a fraction of the lattice vectors in the face-centred lattice of NaCl. The resulting diffraction pattern for the whole crystal structure will be a superposition of all four patterns in Fig. 4, weighted according to the number of Patterson vectors in each set and the appropriate atomic scattering factors. Further, the contribution made by inter-

[4] As discussed in §5.1, thermal vibrations will cause these steps to become rounded off, so that realistic transmittance functions will also be continuous.

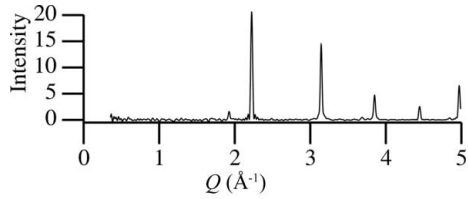

Figure 5
Calculated diffraction pattern for the NaCl crystallite of dimensions $(20\ \text{nm})^3$, as a function of Q. X-ray atomic scattering factors have been applied, but no atomic displacement parameters.

actions of zero length, which sets the background level, must be included. These final steps of the calculation are described in the following section.

2.5. Calculation of the diffraction pattern

The splitting of the Patterson vectors into equivalent sets is necessitated by the inability of the Fourier transformation to accommodate atomic scattering factors that are dependent on Q, as is the case for X-rays. Thus the transforms in Fig. 4 depend merely on atomic coordinates. Atomic scattering information is now included by multiplying the four Fourier transforms of Fig. 4 (i = 1, 4) by the product of the two relevant atomic scattering factors, f_m and f_n. This product is denoted by $f_{mn,i}(Q)$ in equation (5):

$$I^{\text{Debye}}(Q) = \frac{2}{\left[N_{\text{uc}}\, V_{\text{uc}}\right]} \times \left[\sum_i p_i f_{mn,i}(Q)\, F_i^{\text{cs}}(Q) + \frac{1}{2} p_1 f_{mn,1}(Q)\right]. \quad (5)$$

The factor $2/[N_{\text{uc}}\, V_{\text{uc}}]$ leads to units of intensity of electronic units per atom.[5] Factors p_i give the number of equivalent Patterson vectors within set i, with $p_1 = 8$, $p_2 = 24$, $p_3 = 24$ and $p_4 = 8$ here. The second term, $p_1 f_{mn,1}(Q)$, accommodates the contribution to the diffracted intensity made by all Patterson vectors of set 1 that are added to lattice vectors $[n_x, n_y, n_z]$ = [0,0,0]. Since the resulting interaction lengths are zero, this contribution (of atoms interacting with themselves, therefore with $n = m$) cannot be accommodated in the compound slit functions. Its form results from equation (1), as $\text{sinc}(Qr)$ is equal to one for all values of Q. The resulting diffraction pattern is shown in Fig. 5.

It is noticed how many of the maxima observed in curve 1 of Fig. 4 have been cancelled by negative troughs in curves 2 to 4, whereas other maxima have become stronger. The apparent similarity of curves 1 to 4 in Fig. 3(*a*) and the marked differences in their Fourier transforms in Fig. 4 lead to the conclusion that the fine structure of curves 1 to 4, as shown in Fig. 3(*b*), is responsible for the differences in the transforms.

[5] The factor of 2 in the numerator arises from the convention that each pairwise atomic interaction is counted once in deriving the pair distance histogram (and therefore transmittance function) (Thomas, 2010). However, the DSE demands that each interaction be counted twice.

Table 2
Convergence lengths of the sums of equation (7) for three different crystallite sizes of NaCl, together with sum values at the Bragg condition (Q^*) for {200} reflections.

Sum values at Q values displaced by $\pm\Delta Q$ from the Bragg condition (ΔQ = 0.005 Å^{-1}) are quoted as percentages of the value at the Bragg condition.

	Crystal length (nm)		
	20	40	60
R_{max} 1 (Å)	330.530	672.440	1024.115
R_{max} 2 (Å)	332.175	674.075	1025.750
R_{max} 3 (Å)	333.815	675.705	1027.380
R_{max} 4 (Å)	332.220	677.320	1029.000
Convergence length 1 (Å)	257.445	545.080	849.670
Convergence length 2 (Å)	257.400	545.105	849.670
Convergence length 3 (Å)	257.475	545.080	849.690
Convergence length 4 (Å)	257.460	545.130	849.650
$F_1^{cs}(Q^*)$ {200}	1.5330	3.5568	5.6597
$F_1^{cs}(Q^*-\Delta Q)$ {200} (%)	88.1	66.8	39.3
$F_1^{cs}(Q^*+\Delta Q)$ {200} (%)	91.6	68.8	40.6
$F_2^{cs}(Q^*)$ {200}	2.0352	4.0900	6.2392
$F_2^{cs}(Q^*-\Delta Q)$ {200} (%)	91.4	69.7	42.3
$F_2^{cs}(Q^*+\Delta Q)$ {200} (%)	93.3	73.6	46.4
$F_3^{cs}(Q^*)$ {200}	2.0108	4.0690	6.2227
$F_3^{cs}(Q^*-\Delta Q)$ {200} (%)	90.8	69.6	42.5
$F_3^{cs}(Q^*+\Delta Q)$ {200} (%)	93.7	73.3	45.6
$F_4^{cs}(Q^*)$ {200}	2.0315	4.1083	6.2491
$F_4^{cs}(Q^*-\Delta Q)$ {200} (%)	91.1	69.8	43.3
$F_4^{cs}(Q^*+\Delta Q)$ {200} (%)	93.3	73.7	46.5

2.6. A radius-dependent analytical expression for the Fourier transform of a transmittance function

The representation of crystal structural information as a set of transmittance functions, rather than as a set of pair distance histograms, opens up analytical possibilities that arise from the linearity of the Fourier transform. Whereas the compound slit function for each set of Patterson vectors is effectively derived by laying the set of pairwise interaction lengths down horizontally, as shown in Fig. 2(*b*), the same slit function could equally well have been assembled as a sum of pairs of vertical slits (Fig. 6).

This approach offers more flexibility in handling the transmittance function analytically, since its component parts are now identified with narrow ranges of bin number, or equivalently interaction radius. The FT of a double slit has the analytical form derived in equation (6):

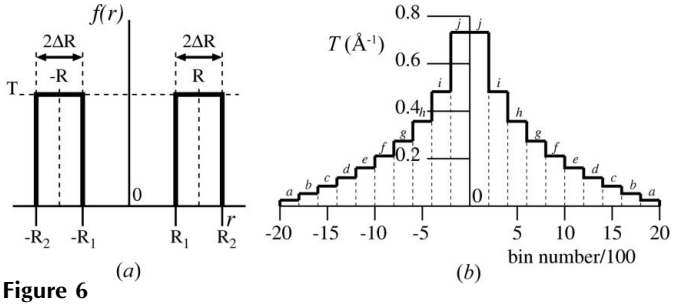

Figure 6
(*a*) A double slit of transmittance T characterized by fundamental parameters R_1 and R_2 and derived parameters R and ΔR. (*b*) Representation of a compound slit function (as in Fig. 2*b*) as a set of double slits. Members of each pair of slits are denoted by the same letter.

$$F^{ds}(Q) = \int_{-R_2}^{-R_1} T\exp(-iQr)\,dr + \int_{R_1}^{R_2} T\exp(-iQr)\,dr$$
$$= \frac{4T}{Q}\cos\left[Q\left(\frac{R_1+R_2}{2}\right)\right]\sin\left[q\left(\frac{R_2-R_1}{2}\right)\right]$$
$$= \frac{4T}{Q}\cos(QR)\sin(Q\Delta R). \quad (6)$$

Thus the FT of a compound slit function may equivalently be evaluated as the sum of $F^{ds}(Q)$ terms, one per contributing double slit [equation (7)]:

$$F_i^{cs}(Q) = \sum_{j=1}^{N} F_i^{ds}(Q)$$
$$= \frac{4}{Q}\sum_{j=1}^{N} T_{ij}\cos(QR_{ij})\sin(Q\Delta R_{ij}). \quad (7)$$

Here index i takes on values from 1 to 4, corresponding to the four sets of Patterson vectors. Index j identifies the contributing double slit, and therefore applies to transmittance T_{ij}, slit mid-point R_{ij} and slit half-width ΔR_{ij} (Fig. 6).

2.7. Applications of equations (5) and (7)

2.7.1. Convergence of the Debye sum. According to equation (7), Fourier transform i at value Q is given by a sum over all double slits of the product of $\cos(QR_{ij})$ and the factor $(4T/Q)\sin(Q\Delta R_{ij})$. The different behaviour of these two factors as values R_{ij} increase is significant. Whereas the $\cos(QR_{ij})$ factor oscillates strongly with increasing R_j for all relevant values of Q, the second factor tends to zero at higher R values. This is due to the fall-off of transmittance values T towards zero at large radius (Fig. 3*a*). Values of $\sin(Q\Delta R_{ij})$ are predominantly positive in the Q range of interest, since ΔR_{ij} values are generally too small to take the argument of the sine function outside the range $0 < Q\Delta R_{ij} < \pi$. Thus, the decay of the amplitude-modulating function $(4T/Q)\sin(Q\Delta R_{ij})$ with increasing radius leads to a convergence of the sums represented by equation (7), as illustrated for three different combinations of Q and i in Fig. 7.

The Q value chosen for Fig. 7(*a*) corresponds to a point in the background of the diffraction pattern, whereas Q values for Figs. 7(*b*) and 7(*c*) correspond to lattice planes {100} and {210} of NaCl, whose reflections are systematically absent. The rate at which the transmittance function $T(r)$ of the compound slit decays to zero depends on the crystallite size. The smaller the crystal, the faster the decay, since factors $|N_x|/L_x$, $|N_y|/L_y$, $|N_z|/L_z$ of equation (2) increase faster when L_x, L_y, L_z are smaller. It is expedient for comparative purposes to define the convergence length of a sum as the smallest value of double-slit half-separation, R, for which all further developing sum values lie within 0.1% of its final value (Fig. 7). Values of this length are quoted in Table 2 for crystallites of length 20, 40 and 60 nm.

Pairwise interactions of radii longer than the applicable convergence lengths affect the transmittance functions merely by slightly raising their overall heights. Since the fine structure

Table 3
Calculation of the theoretical height of the {200} reflection for a crystallite of volume $(20\ \text{nm})^3$.

$Q^* = 2.22804\ \text{Å}^{-1}$; X-ray scattering-factors: $f_{\text{Na}} = 8.64877$; $f_{\text{Cl}} = 12.69794$.

I	$F_i^{\text{cs}}(Q^*)$	$m\cdots n$	$f_{mn,i}$	p_i	Contribution to sum of equation (5)
1	1.5330	$\frac{1}{2}$(Na$\cdots$Na+Cl$\cdots$Cl)	118.019	8	1447.39
2	2.0352	Na$\cdots$Cl	109.822	24	5364.23
3	2.0108	$\frac{1}{2}$(Na$\cdots$Na+Cl$\cdots$Cl)	118.019	24	5695.50
4	2.0315	Na$\cdots$Cl	109.822	8	1784.83
Background	0.5	$\frac{1}{2}$(Na$\cdots$Na+Cl$\cdots$Cl)	118.019	8	472.076
Sum					14764.0

is no longer important, the approximation of a continuum could be used for these long-radius interactions, in order to compute this height correction. Such considerations, which are relevant for an optimization of computational speed, are reserved for future work.

Also quoted in Table 2 are values of the four Fourier transforms at Q values corresponding to the Bragg condition for {200} reflections ($Q^* = 2.22804\ \text{Å}^{-1}$), together with transform values at Q values displaced by $\pm 0.005\ \text{Å}^{-1}$ from the Bragg condition. These indicate the influence of crystallite size on peak height and width, with peak heights observed to rise with increasing crystal length. Conversely the relative peak width is seen to fall with increasing crystal length, with this fall-off slightly less for positive deviations of Q from the maximum intensity at Q^*. This conclusion is underpinned by the values of $F_i^{\text{cs}}(Q^* + \Delta Q)$ typically being 2 or 3% larger than those of $F_i^{\text{cs}}(Q^* - \Delta Q)$.

2.7.2. Embedding the DSE method within the reciprocal-lattice–structure-factor approach to powder diffraction. Since the form of equation (7) allows partial diffraction patterns, $F_i^{\text{cs}}(Q)$, to be calculated with as fine a mesh of Q values as desirable, it is ideally suited, in combination with equation (5), for an accurate calculation of the heights and areas of individual Bragg peaks. This is demonstrated in Table 3 for the {200} reflection, utilizing data from Table 2.

The sum of 14764.0 is then multiplied by the factor $2/[N_{\text{uc}}\, V_{\text{uc}}]$, which is equal to $1.3934 \times 10^{-3}\ \text{Å}^{-3}$ for NaCl, to give the result 20.572 electronic units per atom. This is in agreement with the intensity of the peak at $Q = 2.22804\ \text{Å}^{-1}$ in Fig. 5.

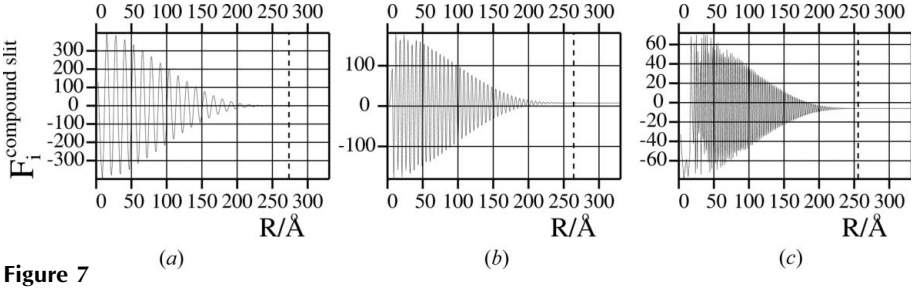

Figure 7
Graphical demonstration of the convergence of the sums in equation (7) (*a*) for $Q = 0.5$ and $i = 1$; (*b*) for $Q = 1.11402$ and $i = 1$; (*c*) for $Q = 2.491025$ and $i = 4$. The convergence length shown by a dashed vertical line corresponds to the smallest R value for which all further values of the developing sum lie within 0.1% of its final value.

With respect to peak areas, the DSE-based approach can be linked with results from the reciprocal-lattice–structure-factor approach to powder diffraction. According to this, the intensity of the *hkl* Bragg reflection is proportional to $Lm_{hkl}\,|F(hkl)|^2$, with L the Lorentz–polarization factor, m_{hkl} the multiplicity of the reflection and the structure factor $F(hkl)$ defined as in equation (8):

$$F(hkl) = \sum_i f_i \left\{ \exp\left[2\pi i (h\, x_i + k\, y_i + l\, z_i)\right] \right\}. \qquad (8)$$

The Lorentz–polarization factor for Bragg powder diffraction, $(1 + \cos^2 2\theta)/(2\sin^2\theta \cos\theta)$, is made up of three components, a polarization factor (for X-rays, but not neutrons) of $(1 + \cos^2 2\theta)/2$, an orientation factor $1/(\sin\theta)$ and the ring factor $1/(\sin\theta\cos\theta)$. The latter two factors, which result from the geometry of diffraction, are not relevant for the DSE method, since the intensity scattered in a single direction is calculated here (Guinier, 1963; Warren, 1969). Consequently the integrated area of a Bragg-peak *hkl*, $\int_{(2\theta)_1}^{(2\theta)_2} I(2\theta)\,\mathrm{d}(2\theta)$, such as may be compared with a DSE-derived integrated peak area, is proportional to $[m_{hkl}\,|F(hkl)|^2]/(\sin^2\theta_{\text{B}}\cos\theta_{\text{B}})$. If Q is used instead of 2θ as the variable of integration, the integral $\int_{(2\theta)_1}^{(2\theta)_2} I(2\theta)\,\mathrm{d}(2\theta) = 2\int_{Q_1}^{Q_2} I(Q)(\mathrm{d}\theta/\mathrm{d}Q)\,\mathrm{d}Q = (\lambda/2\pi)\int_{Q_1}^{Q_2} I(Q)(1/\cos\theta)\,\mathrm{d}Q$. This is approximately proportional to $(1/\cos\theta_{\text{B}})\int_{Q_1}^{Q_2} I(Q)\,\mathrm{d}Q$, with the approximation made that $\cos\theta_{\text{B}}$ is representative of all values of $\cos\theta$ within the range of integration. Since $\sin^2\theta_{\text{B}}$ is proportional to $(Q^*)^2$, the following link between multiplicity, structure factor and integrated DSE-derived reflection intensity follows:

$$\frac{m_{hkl|F(hkl)|^2}}{(Q^*)^2} \simeq k \int_{Q_1}^{Q_2} I(Q)\,\mathrm{d}Q. \qquad (9)$$

Here k is a constant of proportionality that is undetermined. This relationship is validated in Table 4, where the integrated intensities for the eight Bragg maxima at Q values of up to $5\ \text{Å}^{-1}$ are quoted for three different crystallite lengths. Neutron scattering lengths have been used for this purpose, since they are independent of Q. Factors $[m_{hkl}\,|F(hkl)|^2]/(Q^*)^2$ have been calculated *via* the structure-factor method [equation (8)], whereas integrals $\int_{Q_1}^{Q_2} I(Q)\,\mathrm{d}Q$ have been calculated *via* the DSE method, *i.e.* by applying equations (7) and (5) and a step size in Q of $0.0001\ \text{Å}^{-1}$.

Limits of integration Q_1 and Q_2 were fixed in an automated computational procedure, in which intensity values were monitored to lower and higher angles, respectively, proceeding from the Bragg maxima. Both limits were fixed either as the points at which the intensity curve crossed the Q axis, or at the first minima to both sides of the Bragg peaks, whichever came first. The 24 data points in Table 4 give rise to a constant of proportionality, k, of value $(1.430 \pm 0.064) \times 10^{-4}$, thereby confirming the essential correctness of

Table 4
Values of $[m_{hkl}\,|F(hkl)|^2]/(Q*)^2$ and $\int_{Q_1}^{Q_2} I(Q)\,\mathrm{d}Q$ calculated for NaCl crystallites of length 20, 40, 120 nm, utilizing neutron scattering lengths.

The $\langle k\rangle$ value of a reflection is constant k averaged over the three crystallites.

hkl	m_{hkl}	Q^* (Å^{-1})	$F(hkl)$	$[m_{hkl}\,\lvert F(hkl)\rvert^2]/(Q*)^2$	$\int_{Q_1}^{Q_2} I(Q)\,\mathrm{d}Q$			$\langle k\rangle$ (10^4)
					20 nm	40 nm	120 nm	
111	8	1.92954	23.788	1215.9	0.08629	0.08627	0.08597	1.411
200	6	2.22804	52.828	3373.1	0.22941	0.22988	0.23136	1.465
220	12	3.15093	52.828	3373.1	0.24244	0.24102	0.24148	1.396
311	24	3.69479	23.788	999.83	0.07090	0.06587	0.06710	1.471
222	8	3.85908	52.828	1499.2	0.10552	0.10504	0.10210	1.438
400	6	4.45608	52.828	843.28	0.05956	0.05890	0.05748	1.438
331	24	4.85590	23.788	575.95	0.04500	0.04388	0.04406	1.300
420	24	4.98205	52.828	2698.5	0.17764	0.17790	0.17820	1.517

equation (9) in linking the DSE and structure-factor methods. It is anticipated that a more refined treatment would lead to a smaller standard deviation in k.

2.7.3. The derivation of Bragg reflection profiles for nanocrystallites by interpolation. Since the variation in Bragg reflection profiles is most marked for nanocrystallites, the DSE method can be used to good effect here. Since the *nano* region is conventionally taken as encompassing particle sizes of up to 100 nm, this corresponds to up to 177 unit-cell lengths of NaCl. The {220} reflection was selected as an example, and its X-ray profile calculated for cubic crystallites of lengths 20, 40, 80, 160, 320 and 640 unit cells. Transmittance functions were calculated computationally and their Fourier transforms calculated analytically by means of equation (7). Thus exact values of $\cos(QR_{ij})$ and $\sin(Q\Delta R_{ij})$ were calculated at equally spaced values of Q about the Bragg maximum at Q^* = 3.15093 Å^{-1}. Calculations of peak heights, $I_{\max}$, revealed them to be proportional to the crystallite length, L. Results for the reflection profiles are shown in Fig. 8, these being intrinsic, since no account of extrinsic diffractometer-related influences has been made (see §5.2).

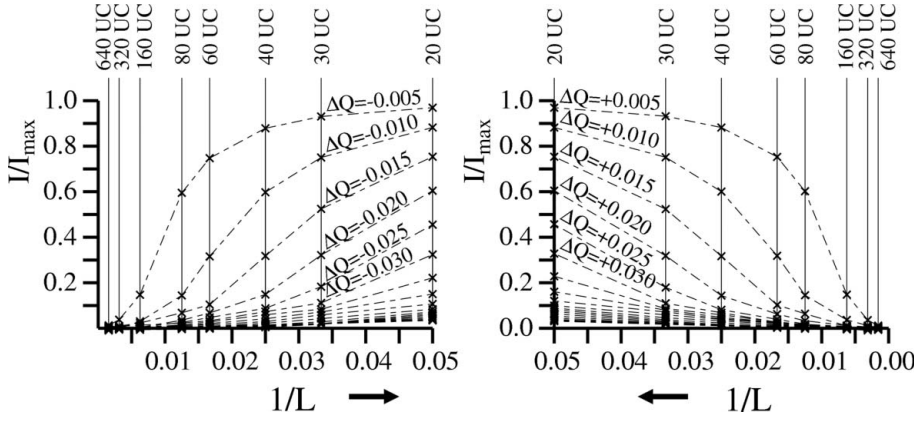

Figure 8
DSE-derived data points (crosses) for the {220} intrinsic reflection profile of cubic crystallites of sodium chloride (X-radiation). Crystallite length L is expressed as the number of unit cells (UC). (*a*) Relative intensity as a function of inverse crystallite length and deviation ΔQ ($0.005 \le |\Delta Q| \le 0.100$) to the left-hand side of the reflection maximum. (*b*) As (*a*), but with ΔQ to the right-hand side of the reflection maximum. The crosses are linked by straight lines, indicating approximate curve profiles.

The systematic development of the curves in Fig. 8 as a function of crystallite length and deviation from the reflection maximum, ΔQ, suggests that curve profiles could be generated for all crystallites within the nanocrystalline size range by a process of interpolation. Further sets of curves for non-cubic crystal habits could likewise be generated.

The application of equations (2), (5) and (7) allows the rapid calculation of intrinsic reflection profiles for all nanocrystallites on a conventional PC. For larger crystallites, the rate-determining step is the calculation of the compound slit functions, since Fourier transformation proceeds rapidly by FFT methods. For this reason, it is shown in the following section how crystallographic symmetry can be exploited in order to expedite these calculations.

3. Symmetry-optimized calculation of compound slit functions

In the earlier work (Thomas, 2010), the sole method of acceleration was the splitting of the pairwise interactions into lattice and Patterson vectors. However, use can also be made, for this purpose, of the Patterson space-group symmetry that is common to both types of vectors. Whereas the high symmetry of NaCl permits the intuitive division of the 64 Patterson vectors into four sets, it is necessary to proceed more systematically for systems of lower symmetry.

The existence of crystal symmetry, in general, gives rise to equivalent lattice vectors. Any two lattice vectors may be regarded as *equivalent* if they give rise to identical sets of interatomic distances in conjunction with a given set of Patterson vectors. In the case of NaCl, these correspond to the 2^3 permutations $[\pm u, \pm v, \pm w]$ coupled with six transpositions of u, v and w between the x, y and z axes, giving rise to sets of up to 48 equivalent lattice vectors. The identification of sets of

Table 5
Generation of the 12*j* and 24*r* positions of space groups 164 and 191 by means of symmetry operator S_1 with two and four generating vectors, respectively.

The numbers in parentheses refer to the general positions as listed in *International Tables for Crystallography* (Hahn, 1995). SG = space group.

Key	Start of closed path (generating) Vector 1	S_1 Vector 2	S_1S_1 Vector 3	$S_1S_1S_1$ Vector 4	$S_1S_1S_1S_1$ Vector 5	$S_1S_1S_1S_1S_1$ Vector 6
SG 164 12*j*/SG 191 24*r*	(1)/(1)	(8)/(14)	(3)/(3)	(7)/(13)	(2)/(2)	(9)/(15)
	x, y, z	$y, \overline{x}+y, \overline{z}$	$\overline{x}+y, \overline{x}, z$	$\overline{x}, \overline{y}, \overline{z}$	$\overline{y}, x-y, z$	$x-y, x, \overline{z}$
SG 164 12*j*/SG 191 24*r*	(4)/(7)	(12)/(21)	(5)/(8)	(10)/(19)	(6)/(9)	(11)/(20)
	$y, x, \overline{z}$	$x, x-y, z$	$x-y, \overline{y}, \overline{z}$	$\overline{y}, \overline{x}, z$	$\overline{x}, \overline{x}+y, \overline{z}$	$\overline{x}+y, y, z$
SG 191 24*r*	(4)	(17)	(6)	(16)	(5)	(18)
	$\overline{x}, \overline{y}, z$	$\overline{y}, x-y, \overline{z}$	$x-y, x, z$	$x, y, \overline{z}$	$y, \overline{x}+y, z$	$\overline{x}+y, \overline{x}, \overline{z}$
SG 191 24*r*	(10)	(24)	(11)	(22)	(12)	(23)
	$\overline{y}, \overline{x}, \overline{z}$	$\overline{x}, \overline{x}+y, z$	$\overline{x}+y, y, \overline{z}$	y, x, z	$x, x-y, \overline{z}$	$x-y, \overline{y}, z$

equivalent lattice vectors is expounded in the following section.

3.1. Identification of equivalent lattice vectors

The combination of lattice vectors with Patterson vectors to produce interaction distances is given in Fig. 9, where a collinear vector set with four elements is shown.

For a given pair of Patterson vectors of equal length ($r_P = p_+ = p_-$), a particular value of $d_{P||}$ is associated with a fixed value of $d_{P\perp}$. Thus the two interatomic distances arising from the pair of Patterson vectors are obtained by applying the theorem of Pythagoras [equation (10)]:

$$r_{\text{interatomic}} = \left[(r_L \pm d_{P||})^2 + r_P^2 - d_{P||}^2\right]^{1/2}. \qquad (10)$$

A set of equivalent lattice vectors is associated with constant values of r_L and r_P, with each member of the set giving rise to the same set of $d_{P||}$ values, and therefore interatomic distances. Calculation of the values of $d_{P||}$ is dependent on crystal symmetry, with the simplest case corresponding to cubic symmetry [equation (11)]:

$$d_{P||} = \frac{a^2\left|ux_P + vy_P + wz_P\right|}{r_L}. \qquad (11)$$

Here u, v, w are the three integers defining the lattice vector of length $r_L = a(u^2+v^2+w^2)^{1/2}$. The Patterson vector is represented as fractional coordinates $[x_P, y_P, z_P]$. Equation (11) allows sets of equivalent lattice vectors with up to 48 members to be identified for NaCl. The identification of sets of equivalent lattice vectors in all the other crystal systems apart from triclinic (for which no symmetry optimization is possible) is simplified by the existence of a unique axis. This is demonstrated for α- and β-quartz, to which trigonal and hexagonal symmetry apply, respectively.

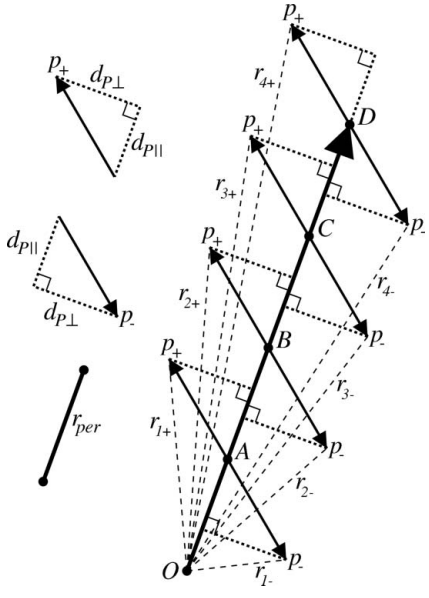

Figure 9
The interatomic distances r_{n+}, r_{n-} (n = 1 to 4) resulting from the addition of a pair of Patterson vectors, p_+ and p_-, with four collinear lattice vectors, OA, OB, OC and OD of periodic distance r_{per}. All eight distances can be generated from the three parameters, r_{per}, $d_{P||}$ and $d_{P\perp}$.

3.1.1. Low and high quartz structures. The room-temperature structure proposed by Kihara (1990) is taken for α-quartz, to which the trigonal space group $P3_221$ (No. 154) applies. This has Patterson symmetry $P\overline{3}m1$, corresponding to space group 164. Similarly the hexagonal structure proposed by him for left-handed β-quartz at 1078 K is taken as a basis, to which space group $P6_222$ (No. 180) applies. The corresponding Patterson symmetry is *P*6/*mmm* (space group 191). A practicable approach to symmetry optimization requires that closed paths be found through the general positions of both space groups. By reference to *International Tables for Crystallography*, Volume A (Hahn, 1995), it may be seen that the 12*j* general positions of space group 164 may be traversed by two closed paths of length six, whereby the symmetry operator between each step, S_1, corresponds to a threefold rotation–inversion operation:

$$S_1 = \begin{pmatrix} 0 & 1 & 0 \\ \overline{1} & 1 & 0 \\ 0 & 0 & \overline{1} \end{pmatrix}.$$

Therefore, two generating vectors are required in order to generate all general positions for α-quartz. Since the maximum closed path length through the 24*r* general positions

Table 6
The 72 Patterson vectors of non-zero length for α- and β-quartz, referred to space groups 164 and 191, respectively.

Interaction	Set	Site	Length	Generating vectors			Lattice translations $[\Delta n_x\ \Delta n_y\ \Delta n_z]$	
			r_P (Å)	x_P	y_P	z_P	2	3
α-Quartz								
Si···O	A	12*j*(1)	1.606	−0.0565	−0.3238	0.1189	[0 1 0]	[0 0 0]
Si···O	B	12*j*(1)	1.606	0.3238	0.0565	0.1189	[0 0 0]	[1 0 0]
Si···O	C	12*j*(2)	3.523	−0.5868	−0.3844	0.4522	[0 0 0]	[0 $\bar{1}$ $\bar{1}$]
Si···O	D	12*j*(2)	3.523	0.3844	0.5868	0.4522	[$\bar{1}$ 0 1]	[0 0 0]
Si···O	E	12*j*(3)	4.108	0.1171	0.8541	0.2144	[$\bar{1}$ $\bar{1}$ 1]	[$\bar{1}$ 0 0]
Si···O	F	12*j*(3)	4.108	−0.8541	−0.1171	0.2144	[0 $\bar{1}$ 0]	[$\bar{1}$ $\bar{1}$ $\bar{1}$]
O···O	G	12*j*(4)	2.646	0.4409	0.1214	0.3333	[0 0 1]	[0 0 0]
O···O	H	12*j*(4)	2.646	−0.1214	−0.4409	0.3333	[0 0 0]	[0 0 $\bar{1}$]
O···O	I	6*i*(1)	2.613	0.2673	−0.2673	0.2378	[0 1 0]	[1 0 0]
O···O	J	6*i*(2)	4.965	0.1459	−0.7082	0.5711	[0 1 0]	[1 0 $\bar{1}$]
O···O	K	6*i*(3)	2.617	0.1736	0.5868	0.0955	[0 $\bar{1}$ 1]	[$\bar{1}$ 0 0]
Si···Si	L	6*i*(4)	3.058	−0.5303	−0.0606	0.3333	[0 $\bar{1}$ 0]	[0 $\bar{1}$ $\bar{1}$]
β-Quartz								
Si···O	A	24*r*	1.587	−0.2922	−0.0843	0.1667	[0 $\bar{1}$ 0]	[0 0 0]
Si···O	B	24*r*	1.587	−0.2079	0.0843	0.1667	[0 0 0]	[0 $\bar{1}$ $\bar{1}$]
Si···O	C	24*r*	1.587	0.2922	0.0843	0.1667	[0 0 0]	[1 0 0]
Si···O	D	24*r*	3.873	−0.7922	−0.0843	0.1667	[0 $\bar{1}$ 0]	[$\bar{1}$ $\bar{1}$ $\bar{1}$]
Si···O	E	6*m*(1)	4.113	0.2922	−0.4157	−0.5	[0 1 0]	[1 0 0]
Si···O	F	6*m*(2)	3.719	0.2922	0.5843	0.5	[0 0 0]	[0 0 0]
O···O	G	12*o*	3.992	0.5843	−0.2079	0.3333	[0 1 0]	[1 0 $\bar{1}$]
O···O	H	12*o*	2.558	−0.2079	0.2079	0.3333	[0 $\bar{1}$ 1]	[$\bar{1}$ 0 0]
O···O	I	12*n*	2.616	0.0	0.3765	0.3333	[0 0 0]	[0 0 1]
O···O	J	12*n*	2.616	0.0	−0.3765	0.3333	[0 0 0]	[0 0 $\bar{1}$]
O···O	K	6*l*	2.603	0.5843	0.1686	0.0	[0 1 0]	[1 0 0]
Si···Si	L	6*i*	3.090	−0.5	0.0	0.3333	[0 $\bar{1}$ 0]	[0 $\bar{1}$ $\bar{1}$]

of space group 191 is also equal to six, the same symmetry operator, S_1, may be used to generate all general positions for β-quartz, starting from four different generating vectors (Table 5).

The Patterson vectors in both structures may accordingly be divided into closed paths with six members, whereby successive vectors within a given closed path are related by the S_1 operator (Table 6).

The information in this table allows all Patterson vectors for α- and β-quartz to be generated. Coordinates in the columns headed x_P, y_P, z_P define the generating vectors, to which the symmetry operations defined in Table 5 are applied. The two columns on the right of Table 6 define additional lattice translations to be applied to Patterson vectors 2 and 3 within the closed paths. These are sometimes required, because the Patterson vectors to be applied to calculate interatomic distances are generated by taking a unit cell with coordinates in the range $0 \leq x, y, z < 1$ and evaluating the differences in x, y, z components between pairs of atoms (Thomas, 2010). The computational method for taking these lattice translations into account is described in the following section.

Patterson vectors 4, 5, 6 in the closed paths are generated by inverting resultant vectors 1, 2 and 3, respectively, in keeping with the symmetry operations of Table 5. For example, the coordinates of the sixth Patterson vector in set C for α-quartz, also taking the additional lattice translation into account, would be calculated analytically as follows:

$$\begin{pmatrix} x_3 \\ y_3 \\ z_3 \end{pmatrix} = \begin{pmatrix} 0 & 1 & 0 \\ \bar{1} & 1 & 0 \\ 0 & 0 & \bar{1} \end{pmatrix} \begin{pmatrix} 0 & 1 & 0 \\ \bar{1} & 1 & 0 \\ 0 & 0 & \bar{1} \end{pmatrix} \begin{pmatrix} -0.5868 \\ -0.3844 \\ 0.4522 \end{pmatrix} + \begin{pmatrix} 0 \\ -1 \\ -1 \end{pmatrix} = \begin{pmatrix} 0.2024 \\ -0.4132 \\ -0.5478 \end{pmatrix},$$

thus $x_6 = -0.2024$; $y_6 = 0.4132$; $z_6 = 0.5478$. The combination of lattice and Patterson vectors is carried out such that the correct interatomic distances result from a minimum of computational effort. It follows from equation (10) that, for given fixed values of r_P and r_L, the appropriate interatomic distance is determined uniquely by the value of $d_{P||}$. If the lattice vectors are grouped into sets of six by successive S_1 operations, just as for the Patterson vectors in Table 5, their common symmetry results in symmetrical matrices of $d_{P||}$ values, as illustrated in Table 7 for one of the Patterson sets of α-quartz, set E of Table 6, in combination with two different sets of lattice vectors, denoted sets 1 and 2.

All 12 lattice vectors, spanning both sets, are of equal length, since the factor $(u^2 + v^2 - uv)$ is invariant. Since a possible orthogonalization matrix for hexagonal axes is:

$$\begin{pmatrix} a & -a/2 & 0 \\ 0 & a(3)^{1/2}/2 & 0 \\ 0 & 0 & c \end{pmatrix}$$

Table 7
Top: Values of $d_{P||}$ obtained for Patterson vector set E of α-quartz in combination with two sets of basal lattice vectors. *Bottom*: Symbolic representation of the six distances $d_{P||}$ that arise with each equivalent lattice vector [°, ⊗, □, -(°), -(⊗), -(□)].

		Set 1			Set 2		
Equivalent lattice vectors in set (1 to 6):		[3 4 0], [4 1 0], [1 $\bar{3}$ 0], [$\bar{3}$ $\bar{4}$ 0], [$\bar{4}$ $\bar{1}$ 0], [$\bar{1}$ 3 0]			[4 3 0], [3 $\bar{1}$ 0], [$\bar{1}$ $\bar{4}$ 0], [$\bar{4}$ $\bar{3}$ 0], [$\bar{3}$ 1 0], [1 4 0]		
Number of S_1 operations on generating Patterson vector	Patterson vector	$d_{P\|\|}$ (Å) with [3 4 0]	Sign in equation (10)	Symbolic representation in matrix	$d_{P\|\|}$ (Å) with [4 3 0]	Sign in equation (10)	Symbolic representation in matrix
0	1	3.070	+	°	1.563	+	°
1	2	3.675	+	⊗	3.914	+	⊗
2	3	0.605	+	□	2.351	+	□
3	4	3.070	−	-(°)	1.563	−	-(°)
4	5	3.675	−	-(⊗)	3.914	−	-(⊗)
5	6	0.605	−	-(□)	2.351	−	-(□)

Patterson vector	1	2	3	4	5	6
1	°	-(□)	-(⊗)	-(°)	□	⊗
2	⊗	°	-(□)	-(⊗)	-(°)	□
3	□	⊗	°	-(□)	-(⊗)	-(°)
4	-(°)	□	⊗	°	-(□)	-(⊗)
5	-(⊗)	-(°)	□	⊗	°	-(□)
6	-(□)	-(⊗)	-(°)	□	⊗	°

the length of a lattice vector $[u, v, w]$ is given by $[a^2(u^2 + v^2 - uv) + c^2 w^2]^{1/2}$. It follows that two lattice vectors will be of equal length if they have w values of equal magnitude, and if the factor $(u^2 + v^2 - uv)$ is equal for both. In this example, three different $d_{P||}$ values arise twice with the first lattice vector of both sets, thereby giving rise to six different interatomic distances per lattice vector, according to the sign within the factor $\left(r_L \pm d_{P||}\right)$ of equation (10). If the six different interatomic distances are denoted by the symbols °, ⊗, □ , -(°), -(⊗), -(□), it is seen in the matrix in the lower part of Table 7 how the symmetry leads to these distances being repeated with other lattice vectors of a given set. Thus the total set of 36 interatomic distances contains just six *different* values, which may be determined from six calculations instead of 36, this representing a sixfold increase in computational efficiency. The geometrical symmetry underpinning Tables 5, 6 and 7 is shown in Fig. 10.

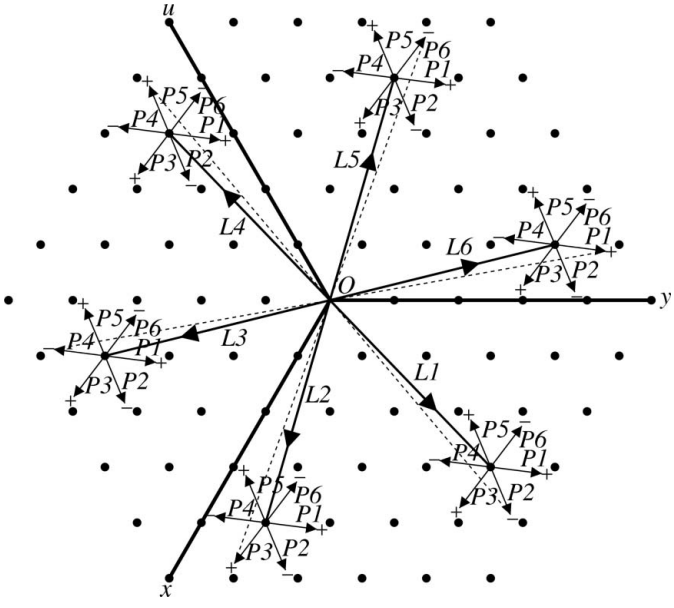

Figure 10
The common symmetry of lattice and Patterson vectors encapsulated by symmetry operator S_1. Lattice vectors $L1$ to $L6$ correspond to the lattice vectors in set 1 of Table 7, with Patterson vectors $P1$ to $P6$ giving rise to the $d_{P||}$ values also listed for this set. Dashed lines indicate one of the six different interatomic distances, this being repeated six times.

3.2. Efficient program architecture

For the six crystal systems with a unique axis, which is taken as z here, it is expedient to sum just the x_P and y_P components of the Patterson vectors with basal lattice vectors, $[n_x, n_y, 0]$, so that the resultant vectors lie within the basal planes. The z components of the Patterson vectors, z_P, are added to z-lattice translations at a later stage. In order to maximize efficiency, collinear basal lattice vectors are taken (as in Fig. 9), with $d_{P||}$ one of the in-plane Patterson vector components. The other in-plane component, $d_{P\perp,xy}$, is readily evaluated as $[r^2_{P,xy} - d^2_{P||}]^{1/2}$ (Fig. 11*a*).

The method for dealing with the x and y components of additional lattice translations $[\Delta n_x\ \Delta n_y\ \Delta n_z]$ of Patterson vectors (see Table 6) is shown in Fig. 11(*b*). For example, Patterson vector 2 of set E of α-quartz ($P2$) is subjected to an additional in-plane translation of $[\bar{1}\ \bar{1}\ 0]$, giving rise to an end-point for the pairwise interaction with lattice vector [3 4 0] that could alternatively have been reached from lattice vector [2 3 0] by means of vector $P2$ alone. In order to exploit the full symmetry computationally, it is necessary to use Patterson vectors $P1$ to $P6$ without additional lattice translations. Thus it is necessary to generate the resulting pairwise distance from lattice vector [2 3 0], and not lattice vector [3 4 0]. The diffi-

culty remains, however, that the frequency of occurrence of the interatomic distance is still determined by lattice vector [3 4 0], which is to be used in connection with equation (2). A similar interpretation applies to Patterson vectors 3, 5 and 6 in Fig. 11(*b*).

This difficulty can be dealt with by modifying equation (2) to give equation (12):

$$N'(n_x, n_y, 0) = \frac{1}{\left[N_{\rm uc}\, V_{\rm uc}\right]}\left(1 - \frac{\left|n_x - \Delta n_x\right|}{L_x}\right)\left(1 - \frac{\left|n_y - \Delta n_y\right|}{L_y}\right). \quad (12)$$

Whereas formerly lattice vector [3 4 0] would have been summed with Patterson vector 2 and an additional lattice translation [$\bar{1}\ \bar{1}$ 1] applied, the lattice vector associated with full symmetry, *i.e.* [2 3 0], is now entered into equation (12): $n_x = 2$, $n_y = 3$, $\Delta n_x = -1$ and $\Delta n_y = -1$. Since factors $|n_x - \Delta n_x|$ and $|n_y - \Delta n_y|$ are equal to 3 and 4, respectively, the correct frequencies are obtained for the resulting interatomic distance generated, without an explicit reference to [3 4 0].

The final set of interatomic distances leading to a compound slit function is generated by combining the in-plane distances with z components. Each in-plane distance forms the base of a right-angled triangle of height given by $[n_z \pm (z_{\rm P} + \Delta n_z)]c$, whose hypotenuse gives the interatomic distance. Here c is the lattice parameter along z and n_z takes on values $0 \le n_z < L_z$ [see equation (2)]. For α- and β-quartz, up to four sets of two-dimensional distances and frequencies for the basal layer need to be stored internally within the program for a given set of Patterson vectors, depending on values of $z_{\rm P}$ and Δn_z (see Table 6). More generally, these z components may correspond to $\pm z_{\rm P}$, $\pm(z_{\rm P} + \Delta n_{z,2})$, $\pm(z_{\rm P} + \Delta n_{z,3})$. These sets are ideally stored as histograms of bin width equal to half the sampling length of 0.01 Å, *i.e.* with bin width 0.005 Å. However, it was found that a bin width of 0.01 Å was adequate, leading to improvements in computational speed without deleterious consequences for the quality of the Fourier-transformed data. Frequencies of the three-dimensional vectors are derived from the in-plane frequencies of equation (12) by multiplying by the factor $(1 - |n_z|/L_z)$ for non-basal lattice vectors [see equation (2)], with the correction factor $\frac{1}{2}$ applied to basal lattice vectors (Thomas, 2010).

In the case of α-quartz, nine compound slit functions were calculated as follows: 1, for lattice vectors alone (or equivalently, for Patterson vectors 000, corresponding to special position 1*a* in space group 164); 2, for sets A and B; 3, for sets C and D; 4, for sets E and F; 5, for sets G and H; 6, for set I; 7, for set J; 8, for set K; 9, for set L (see Table 6). Therefore, nine separate Fourier transformations were subsequently carried out. For β-quartz the number of compound slit functions (and Fourier transforms) to be calculated was one fewer, because sets A, B, C and D, corresponding to special position 24*r* in space group 191, are brought together.

A parallel program architecture was adopted, with nine and eight threads for α- and β-quartz, respectively. By comparison with the earlier code (Thomas, 2010), the adoption of Fourier transform methods allowed a straight-through calculation from Patterson vector set to Fourier-transformed data, without the storage of intermediate histogram sampling data to disk. This led to a marked improvement in computational times (see §3.4). As for NaCl (see §2.4), a sampling length of 0.01 Å led to discrete Q values of spacing 1.198×10^{-3} Å^{-1} for an array size of 2^{19}. However, in order to avoid aliasing effects in the Fourier transforms at low Q values (Press *et al.*, 1996), an array size of 2^{20} was adopted to store the compound slit functions for crystallite lengths in excess of *ca* 150 nm. Here the array elements corresponding to non-existent interactions of higher length were packed with zeroes. Similarly for crystallite lengths in excess of *ca* 320 nm, an array size of 2^{21} was adopted. These array sizes led to a Q spacing of one half and one quarter of the original value, *i.e.* 0.599×10^{-3} and 0.300×10^{-3} Å^{-1}, respectively. The associated increase in computational time for Fourier transformation was minimal (see §3.4).

The actual exploitation of equivalence between lattice vectors within a computer program requires care, since the realization of an equivalence depends on the shape of the

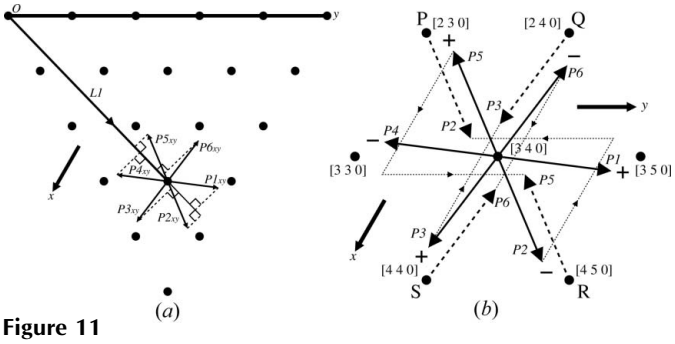

Figure 11
(*a*) Right-angled triangles for calculation of $d_{\rm P||}$ and $d_{{\rm P}\perp,xy}$ values for the set of Patterson vectors of Fig. 10 with respect to lattice vector [3 4 0]. Dashed lines: $d_{{\rm P}\perp,xy}$; solid lines: $d_{\rm P||}$; arrows: projections of Patterson vectors 1 to 6 in the xy plane. (*b*) In-plane treatment of additional lattice translations [$\bar{1}\ \bar{1}$ 1], [$\bar{1}$ 0 0], [1 1 $\bar{1}$] and [1 0 0] (shown as thin dashed lines) connected with Patterson vectors 2, 3, 5 and 6 starting at lattice vector [3 4 0]. The four end-points can alternatively be reached from neighbouring lattice vectors P, Q, R and S by use of Patterson vectors 2, 3, 5 and 6 without the additional translations.

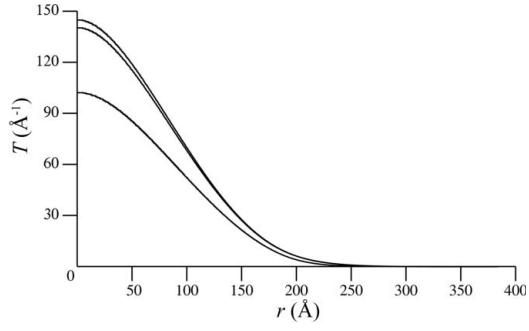

Figure 12
Comparison of compound slit functions for the lattice vectors of NaCl (curve 1 of Fig. 3*a*), α- and β-quartz (curves from top to bottom: α-quartz; β-quartz; NaCl). The lengths of the crystallites are equal to 20 nm along the three crystal axes. The nine Fourier transforms calculated for α-quartz (crystallite length 150 nm along all three axes) are shown in Fig. 13, this being the equivalent of Fig. 4 for NaCl, although for considerably larger crystallites here.

Table 8
Comparison of computational times (in s) and factors of improvement for diffraction patterns of α- and β-quartz as a function of crystallite length.

System	Condition	Crystallite length (nm)								
		40	80	120	160	200	240	280	320	360
β-Quartz	Total	3	10	25	47	81	122	174	236	307
α-Quartz	Total	3	12	30	58	95	142	199	266	347
α-Quartz	FFT	1	1	2	2	3	3	3	3	3
β-Quartz	FFT	1	2	2	2	3	3	3	3	4
α-Quartz	$f_{\rm total}^{\rm hardware+software}$	16.3	10.9	9.2	8.8	9.2				
α-Quartz	$f_{\rm total}^{\rm software}$	8.2	6.9	6.1	6.0	6.3				

crystallite. Within a given set of equivalent collinear lattice vectors, the equivalence can only be exploited for as many elements as are in the *shortest* collinear set. The contributions from higher elements must be calculated explicitly, without reference to equivalences, as one or more symmetrically related partners are missing. These considerations are not important for a cubic crystallite of sodium chloride, but would apply as soon as the crystallite departed from cubicity. By comparison, full symmetrical equivalence for quartz would only be achieved for crystallites of hexagonal habit, and not for prismatic crystallites, to which the results in the following section apply.

3.3. Compound slit functions, Fourier transforms and diffraction patterns obtained for α- and β-quartz

The form obtained for the compound slit functions of α- and β-quartz is qualitatively similar to that of NaCl, as shown in Fig. 12 for crystallites of length 20 nm. Since the height of the maximum at $R = 0$ is given by the sum over all primitive lattice vectors, **r** of factors $1/2|\mathbf{r}|$, as described in §2.2, the fall-off in height from α-quartz through β-quartz to NaCl can be understood from the progressive increase in unit-cell volume, with values of $V_{\rm uc}^{1/3}$ for the three systems equal to 4.8347, 4.9039 and 5.6401 Å, respectively.

The marked increase in peak sharpness compared to Fig. 4 for NaCl is evident, where the associated crystallite length was 20 nm. Conventional diffraction patterns, whereby 2θ is the independent variable instead of Q, are shown in Fig. 14 for α- and β-quartz with crystallite lengths of 20 and 150 nm. Equation (5) has been used here, with a wavelength of 1.54051 Å for Cu $K\alpha_1$ radiation applied, in order to convert from Q to 2θ (Thomas, 2010).

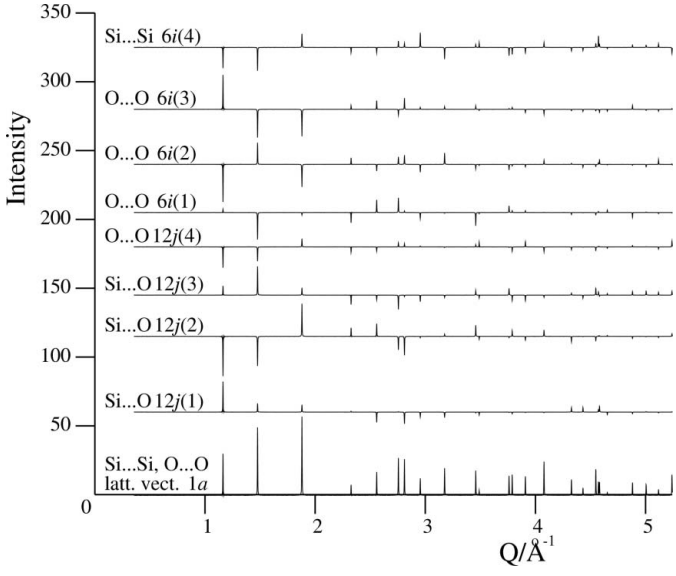

Figure 13
Fourier transforms $F_i^{\rm cs}(Q)$ $(i = 1, 9)$ for the nine symmetry-equivalent sets of Patterson vectors in α-quartz (crystallite length 150 nm). The sets are labelled according to Wyckoff positions in space group 164, as in Table 6.

3.4. Indicative computational times

For the software developed in the course of the current work, total times for full, exact calculations are reported in Table 8 as the condition 'Total'. The condition 'FFT' refers to the Fourier transform part of the calculations, these having been calculated by suppressing the Fourier transform and noting the reduction in overall computational time. The PC used was equipped with an Intel Core 2 Duo processor E8400. The software was written to be used in conjunction with the Intel Fortran compiler, Version 9.0, with dual explicit parallelization achieved by means of the single OpenMP compiler directive c$OMP PARALLEL DO in combination with a dedicated program structure.

Factor $f_{\rm total}^{\rm hardware+software}$ indicates the overall factor of improvement compared to the previous work (Thomas, 2010), this being brought about by migrating from the E6850 to the E8400 processor and by using the software described here. The contribution made by the new software alone is expressed by improvement factor $f_{\rm total}^{\rm software}$, which was derived by running old and new software on an E6850 processor.

Parallelization efficiencies, *i.e.* the extent to which multiple threads create a direct benefit for the computation times, were calculated to vary between 89 and 100%.[6]

The new algorithm has permitted an extension of the sample lengths to 360 nm (and beyond), this being well outside the nanocrystalline range (of up to 100 nm), with computational times comparable to those obtained for crystallites of length L between 120 and 160 nm using the former code. Further, the L^3 dependency associated with the former code has been improved here to an L^n dependency, with $n \simeq 2.30$ for α- and $\simeq 2.23$ for β-quartz. This is attributed to the in-plane summation of lattice and Patterson vectors described in §3.2. The issue of reducing computational times further is discussed in §5.3.

[6] The criterion for monitoring parallelization efficiency was as follows. 100% efficiency is realized when two threads running in parallel achieve a total computation time equal to one half the time taken for serial execution. 0% efficiency is realized when the parallel execution time is equal to the serial execution time. Efficiencies corresponding to intermediate times are calculated by linear interpolation.

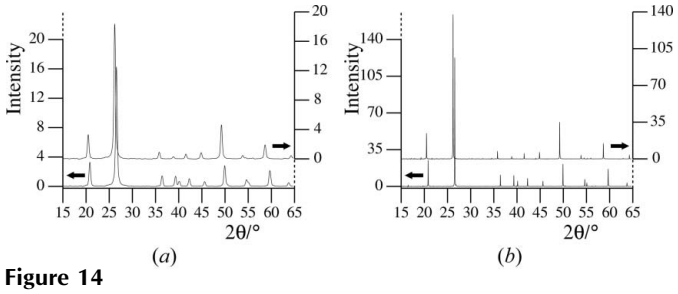

Figure 14
Calculated diffraction patterns for α- and β-quartz with crystallite lengths of (*a*) 20 and (*b*) 150 nm (Cu $K\alpha_1$ radiation; no displacement parameters applied). Lower curves: α-quartz; upper curves: β-quartz.

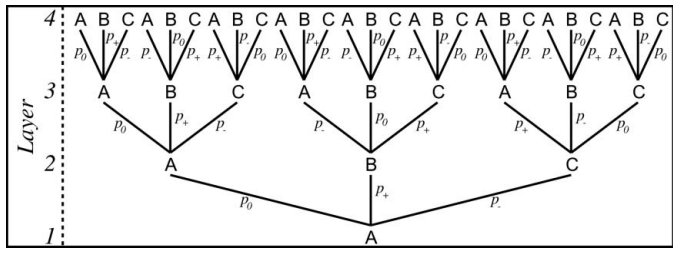

Figure 15
Probability tree for a hypothetical crystallite with four atomic layers, in which three alternative layer positions A, B and C can occur.

A further hidden benefit of using the FFT algorithm, compared to the explicit sine summation used earlier (Thomas, 2010), is its ability to supply diffraction data to much higher Q values at no extra computational cost. This would be relevant for X-ray synchrotron radiation or when using laboratory diffractometers equipped with Mo or Ag anodes. Whereas Cu $K\alpha$ radiation is associated with a Q value of 8.0 Å^{-1} at 160° 2θ, Mo $K\alpha$ and Ag $K\alpha$ radiation give rise to Q values of 17.4 and 22.1 Å^{-1}, respectively. This use of extended 2θ ranges is relevant for conventional p.d.f. work (te Nijenhuis *et al.*, 2009).

As the symmetry-based optimization software has not been developed for Patterson groups other than $P\bar{3}m1$ and $P6/mmm$, it is not yet ready for distribution.

4. Compound slit functions for disordered structures

Whereas the focus until now has been on three minerals exhibiting perfect crystal symmetry, the inherent flexibility of the DSE in handling disorder in crystalline systems is a major motivation for its use as a theoretical basis for powder diffraction. As in the earlier article (Thomas, 2010), the structure of the clay mineral kaolinite is used in order to describe two innovations here, first the use of analytically calculated probabilities to describe stacking faults, and secondly the derivation of compound slit functions for disordered systems.

4.1. Analytically calculated diffraction patterns for planar disordered systems

In the earlier article (Thomas, 2010), the degree of planar disorder in kaolinite was defined in terms of a disorder parameter $\varphi_{\rm dis}$, which was allowed to vary between 0 and 1. It was related to the probabilities of alternative shifts Δy between adjacent layers in a stack. The allowed shifts were $\Delta y = 0, \pm\frac{1}{3}$, with corresponding probabilities denoted by p_0, p_+ and p_- [equation (13)]

$$p_0 = 1 - \frac{2\varphi_{\rm dis}}{3}$$
$$p_+ = p_- = \frac{\varphi_{\rm dis}}{3}. \qquad (13)$$

The construction of a single crystallite, from which to calculate the diffraction pattern, was handled formerly by means of a random-number generator, with the field of the generator between 0 and 1 divided up according to the value of $\varphi_{\rm dis}$. This gave rise to satisfactory results only at the limit of $\varphi_{\rm dis} = 0$, since all random numbers lead to Δy shifts of zero in this case. For non-zero values of $\varphi_{\rm dis}$, however, an element of arbitrariness was introduced by the particular random numbers generated,[7] leading to unsmooth diffraction patterns.

A better approach, which is equivalent to an averaging over many crystallites of equal size, is to calculate the probabilities that a given layer is either A, or B, or C analytically. The method is shown in Fig. 15.

Probability p_0 is associated with A→A, B→B or C→C transitions between adjacent layers. Similarly probability p_+ is associated with A→B, B→C or C→A transitions, and probability p_- with A→C, B→A or C→B transitions between adjacent layers. On this basis, analytical expressions for the probabilities of different layer positions A, B and C may be calculated, as shown in Table 9.

The calculation of analytical probabilities may be extended computationally to any number of atomic layers, since the same principles apply as for these four layers. As a result, the desired smooth gradation in the generated diffraction patterns between complete order and complete disorder is obtained (Fig. 16). Here the range of diffraction angles between 19 and 33° is highlighted, within which a well known feature is the progressive formation of a wedge shape with increasing disorder. These results are to be compared with the noisy diffraction patterns in Figs. 11 and 12 of the earlier article (Thomas, 2010), which resulted from the use of a random-number generator.

4.2. Compound slit functions for kaolinite at varying degrees of disorder

As described earlier (Thomas, 2010), probabilities such as those calculated in Table 9 serve as weights for the relative contributions of three different *total* sets of Patterson vectors. Absolute pairwise layer correlations A→A, B→B or C→C require the use of an unaltered set of Patterson vectors. By

[7] This is an example of the law of large numbers (from probability theory) applying. Use of a random-number generator is equivalent to the rolling of a dice, whereby the cumulative average result of 3.5 is seldom reached quickly.

Table 9
Probabilities of different layer positions in terms of elementary probabilities p_0, p_+ and p_-.

Layer	Probability of layer position A	Probability of layer position B	Probability of layer position C
1	1	0	0
2	p_0	p_+	p_-
3	$p_0^2 + 2\,p_+\,p_-$	$p_-^2 + 2\,p_0\,p_+$	$p_+^2 + 2\,p_0\,p_-$
4	$p_0^2 + p_+^2 + p_-^2 + 6\,p_0\,p_+\,p_-$	$3(p_0^2\,p_+ + p_+^2\,p_- + p_-^2\,p_0)$	$3(p_0^2\,p_- + p_-^2\,p_+ + p_+^2\,p_0)$

comparison, absolute pairwise layer correlations A→B, B→C or C→A require a Patterson vector set in which a translation of $\Delta y = +\frac{1}{3}$ has been applied to each vector. Similarly absolute pairwise layer correlations A→C, C→B or B→A require a set of Patterson vectors to which a translation of $\Delta y = -\frac{1}{3}$ has been applied to each vector.

The presence of translations of this kind destroys the Patterson symmetry of a perfectly ordered crystal. Furthermore, the triclinic symmetry of kaolinite (Bish, 1993) precludes the use of a symmetry-optimized technique for calculating compound slit functions. Therefore the latter were generated from the pair distance histograms obtained with earlier software (Thomas, 2010).

As observed for NaCl, the coarse structure of the transmittance functions is indistinguishable between ordered and disordered kaolinite, whereas considerable variation in the fine structure is observed (Fig. 17). The latter is responsible for the significant differences between the diffraction patterns shown in Fig. 16.

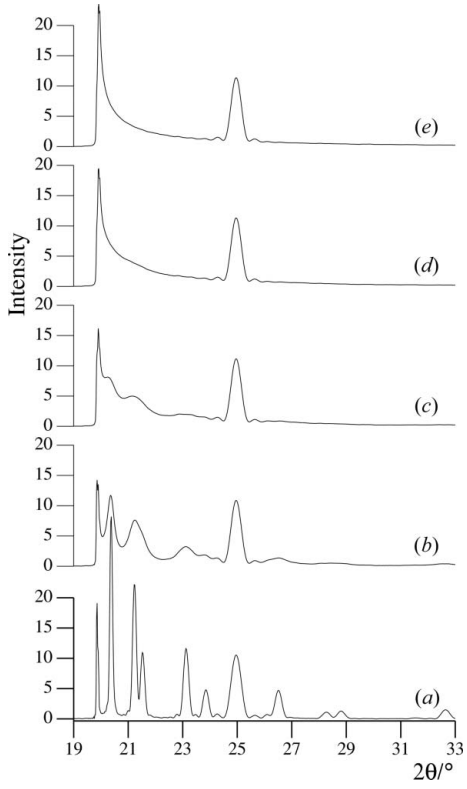

Figure 16
Diffraction patterns for kaolinite generated with analytical probabilities for 2θ angles between 19 and 33° (Cu $K\alpha_1/K\alpha_2$ radiation). The five curves correspond to the following degrees of order: (*a*) 100%; (*b*) 75%; (*c*) 50%; (*d*) 25%; (*e*) 0%.

5. Areas of future work

5.1. The accommodation of atomic displacement parameters in compound slit functions

Since the encoding of crystal structural information in histogram form does not offer a simple means of incorporating atomic displacement factors (ADPs), Debye–Waller factors were applied to the diffraction patterns in the earlier work (Thomas, 2010). This led to the restriction that only isotropic displacement parameters could be applied. By comparison, the encoding of crystal structural information in the form of compound slit functions allows isotropic and anisotropic displacement factors to be accommodated prior to Fourier transformation.

The principle for anisotropic ADPs may be enunciated by considering two atoms, A and B, separated by a length R. As a result of thermally excited atomic vibrations, this single length is replaced by a distribution of lengths about this mean value. A Gaussian function may be used to model this, such that the probability of a length $(R + \Delta R)$ is given by $P_R(\Delta R) = [1/\sigma(2\pi)^{1/2}]\exp(-\Delta R^2/2\sigma^2)$, with σ equal to the r.m.s. displacement $\langle \Delta R^2 \rangle^{1/2}$. Owing to the supine encoding of the pairwise interactions within a compound slit function, the Gaussian manifests itself in the form of the cumulative distribution function $D_R(\Delta R)$, this being the integral $\int_{-\infty}^{\Delta R} P_R(R')\,\mathrm{d}R'$, with explicit form $(1/2)\{1 + \mathrm{erf}[\Delta R/\sigma(2)^{1/2}]\}$ (Fig. 18*a*).

The inversion of the cumulative distribution function for positive arguments of the transmittance functions may be understood by visualizing that thermal vibrations give rise to smaller interaction lengths, for which $\Delta R < 0$. Thus the transmittance values start to fall off from the higher values of each step sooner. The larger interaction lengths that result from the vibrations lead to the rounding-off of each step at positive ΔR values.

The decision was taken not to develop this approach further within this article, as the derivation of σ values for pairwise

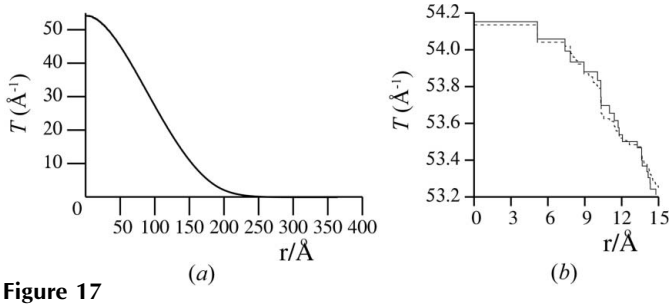

Figure 17
Comparison of compound slit functions for 100% ordered and 100% disordered kaolinite [lattice vectors only; crystallite size (20 nm)^3]. (*a*) Complete, coarse structure (overlaying of two curves); (*b*) fine structure at radii up to 15 Å. Solid line: 100% ordered kaolinite; dashed line: 100% disordered kaolinite.

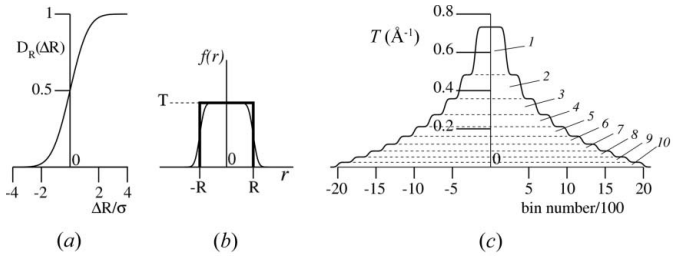

Figure 18
(*a*) Cumulative distribution function $D_R(\Delta R)$; (*b*) rounding-off of the sharp edges of a single slit (*cf.* Fig. 1*a*); (*c*) schematic representation of the rounding-off that occurs within a compound slit function (*cf.* Fig. 2*b*).

interactions from isotropic and anisotropic atomic displacement parameters is non-trivial. This is because the atomic vibrations have components both parallel and perpendicular to the pairwise interaction vectors, which must be appropriately combined to give the correct σ values. Further, a computationally efficient method is required. It is therefore proposed to carry out this work in the future. The procedure to be developed will be validated by requiring that isotropic displacement parameters give rise to identical results by both methods: (i) application of $D_R(\Delta R)$ functions to compound slit functions prior to Fourier transformation; (ii) application of Debye–Waller factors to partial diffraction patterns after Fourier transformation.

5.2. Interaction with experiment

An important insight gained from the current work is that the calculated widths of the Bragg reflections, even for relatively modest crystallite volumes of the order of $(150\ \text{nm})^3$, are similar to those obtained from typical X-ray diffractometers with much larger crystallites. It follows that the experimentally observed width of a given peak results from a convolution of an intrinsic, DSE-calculated peak profile and an instrumental profile $I^{\text{inst}}(Q)$, which is characteristic of the X-ray optical system/neutron beam focusing. As a result of the introduction of Fourier transform techniques in this work, the convolution theorem may be straightforwardly applied in combination with an inverse Fourier transformation, in order to calculate a multiplying function $\Phi(R)$ for the compound slit function [equation (14)]:

$$\mathcal{F}_Q^{-1}\left[F_i^{\text{cs}}(Q)^* I^{\text{inst}}(Q)\right](R) = T_i^{\text{cs}}(R) \times \mathcal{F}_Q^{-1}\left[I^{\text{inst}}(Q)\right](R), \qquad (14)$$

whereby $\Phi(R) = \mathcal{F}_Q^{-1}[I^{\text{inst}}(Q)](R)$. Here $F_i^{\text{cs}}(Q)$ represents the forward Fourier transform of the transmittance function $T_i^{\text{cs}}(R)$ of Patterson set i (as in Figs. 3, 12 and 17). The use of a function $\Phi(R)$ would mean that the compound slit functions could be converted to a form directly applicable to the experimental configuration prior to Fourier transformation. This proposed method is in need of experimental verification.

A further area of dialogue with experiment concerns the effects on peak profiles brought about by variable crystallite habits. Since the DSE is inherently capable of accommodating all such morphological considerations, it is anticipated that its use will ultimately provide more flexibility than methods based, for example, on use of the Caglioti function (Caglioti *et al.*, 1958).

5.3. The further reduction of computational times

It is thought that the calculation principles described in this article, *i.e.* the use of fast Fourier transforms and the exploitation of crystal symmetry, indicate how the exact value of the Debye sum may be calculated most efficiently. Since §3.4 has revealed the strong dependence of calculation time on processor, it follows that further progress in reducing computational times for the exact sum will require the migration to a more powerful processor and/or the use of parallel processors.

Nevertheless there is still potential for the use of appropriate time-saving approximations, this being a subject that has only been touched upon in §2.7.1. Here it was shown that convergence lengths may be defined when equation (7) is used to calculate diffraction patterns. Particularly elegant would be the capability of using convergence *acceleration* techniques, such that the high-R end-values observed, for example, in Fig. 7 could be calculated merely from the oscillatory behaviour at low R.[8]

It has been seen in Fig. 14(*b*) that a crystallite length of 150 nm for α- and β-quartz already leads to sharp diffraction peaks. The question therefore arises as to whether an increase in calculation time by a factor of *ca* 7 for a sample length of 360 nm is justifiable, given that the resulting diffraction patterns will be so similar. Furthermore, the peak-broadening instrumental contribution could mean that exact calculations for high sample lengths prove to be superfluous, in particular if the convolution approach expressed by equation (14) is successful.

5.4. The inverse Fourier transform

It has been shown that powder diffraction is yet another potential area of application of the one-dimensional fast Fourier transform. By their nature Fourier transforms are two-way. The experimental data arising from 'real' samples, *i.e.* multiphase with a grain size distribution, could be inverse Fourier transformed to give rise to a superposition of transmittance functions. Since the coarse structure of an elementary transmittance function is characteristic of the phase from which it is derived (as determined by the unit-cell parameters) and the grain size (see Fig. 12), the technique of inverse Fourier transformation of experimentally derived diffraction patterns could well find application in quantitative phase analysis and in the determination of particle size distributions by X-ray diffraction. With respect to the quantitative phase analysis of clays, the insensitivity of the coarse structure of the transmittance functions to disorder (see Fig. 17*a*) may facilitate quantitative determination of the concentration of

[8] A further contribution to reducing computational time could also be achieved by methods similar to those advocated by Cervellino *et al.* (2006).

kaolinite by powder diffraction, irrespective of the degree of disorder.

Dr Milen Gateshki of PANalytical B.V. in Almelo is thanked for helpful discussions.

References

Beyerlein, K., Cervellino, A., Leoni, M., Snyder, R. L. & Scardi, P. (2009). *Z. Kristallogr. Suppl.* **30**, 85–90.

Bish, D. L. (1993). *Clays Clay Miner.* **41**, 738–744.

Caglioti, G., Paoletti, A. & Ricci, F. P. (1958). *Nucl. Instrum. Methods Phys. Res. Sect. A*, **3**, 223–226.

Cervellino, A., Giannini, C. & Guagliardi, A. (2006). *J. Comput. Chem.* **27**, 995–1008.

Cervellino, A., Giannini, C. & Guagliardi, A. (2010). *J. Appl. Cryst.* **43**, 1543–1547.

Farrow, C. L., Juhas, P., Liu, J. W., Bryndin, D., Božin, E. S., Bloch, J., Proffen, T. & Billinge, S. J. (2007). *J. Phys. Condens. Matter*, **19**, 335219.

Gelisio, L., Azanza Ricardo, C. L., Leoni, M. & Scardi, P. (2010). *J. Appl. Cryst.* **43**, 647–653.

Guinier, A. (1963). *X-ray Diffraction in Crystals, Imperfect Crystals and Amorphous Bodies*, pp. 5–9, 49–51. San Francisco: W. H. Freeman.

Hahn, T. (1995). Editor. *International Tables for Crystallography*, Vol. A, *Space-Group Symmetry*. Dordrecht: Kluwer.

Hall, B. D. & Monot, R. (1991). *Comput. Phys.* pp. 414–417.

Kihara, K. (1990). *Eur. J. Mineral.* **2**, 63–77.

Lipson, S. G. & Lipson, H. (1981). *Optical Physics*, 2nd ed., pp. 157–160. Cambridge University Press.

Nijenhuis, J. te, Gateshki, M. & Fransen, M. (2009). *Z. Kristallogr. Suppl.* **30**, 163–169.

Press, W. H., Teukolsky, S. A., Vetterling, W. T. & Flannery, B. P. (1996). *Numerical Recipes in Fortran 77: the Art of Scientific Computing*, 2nd ed., pp. 494–508. Cambridge University Press.

Thomas, N. W. (2010). *Acta Cryst.* A**66**, 64–77.

Walker, D., Verma, P. K., Cranswick, L. M. D., Jones, R. L., Clark, S. M. & Buhre, S. (2004). *Am. Mineral.* **89**, 204–210.

Warren, B. E. (1969). *X-ray Diffraction*, pp. 47–49. Massachusetts: Addison-Wesley.